Frontiers in Bioscience Landmark

*Front. Biosci. (Landmark Ed)* **2026**; 31(8): 52978
https://doi.org/10.31083/FBL52978

*Original Research*

# Reverse Network Pharmacology–Based Identification of 20-Hydroxyecdysone and Its Inhibition of Glioblastoma Malignant Phenotypes Through the PI3K/AKT Pathway

Jinhui Zhang[1,2], Chao Wei[3], Dongyan Wang[3], Renmi He[3], Xiangdan Xiao[3], Jianwei Xu[1,2,*], Junhou Lu[1,2,*]

[1]Center for Tissue Engineering and Stem Cell Research, Translational Medicine Research Center, Guizhou Biomanufacturing Laboratory, Guizhou Medical University, 561113 Guiyang, Guizhou, China
[2]Department of Pharmacology, School of Basic Medicine, Guizhou Medical University, 550025 Guiyang, Guizhou, China
[3]Department of Physiology and Pathophysiology, School of Basic Medicine, Guizhou Medical University, 550025 Guiyang, Guizhou, China
*Correspondence: xujianwei@gmc.edu.cn (Jianwei Xu); lujunhou@gmc.edu.cn (Junhou Lu)
Academic Editor: Qingping Dou
Submitted: 16 April 2026 Revised: 5 June 2026 Accepted: 12 June 2026 Published: 18 August 2026

**Abstract**

**Background:** Glioblastoma is the most aggressive primary malignant brain tumor of the central nervous system and remains difficult to treat because of rapid progression, diffuse invasion, and frequent recurrence. This study aimed to identify a potential natural compound against glioblastoma using a reverse network pharmacology strategy and to investigate its anti-glioma effects and underlying mechanism. **Methods:** Glioblastoma-related targets were collected from public disease databases and integrated with differentially expressed genes from a public transcriptomic dataset to identify intersecting targets. Protein-protein interaction analysis, hub target screening, functional enrichment analysis, and reverse network pharmacology were performed to identify candidate compounds. Molecular docking and 100-ns molecular dynamics simulations were used to assess interactions between 20-hydroxyecdysone and pathway-related targets. Cell viability, colony formation, apoptosis, migration, and protein expression were examined in U251 and U87 glioma cells. Statistical differences were analyzed using a paired Student's *t*-test for two-group comparisons or one-way analysis of variance (ANOVA) followed by Dunnett's multiple-comparisons test for multi-group comparisons, as appropriate. **Results:** A total of 136 intersecting targets and 18 hub targets were identified. Functional enrichment analysis indicated that the phosphatidylinositol 3-kinase/protein kinase B signaling pathway was one of the key enriched pathways. Reverse network pharmacology identified 20-hydroxyecdysone as a candidate compound. Molecular docking showed relatively strong binding of 20-hydroxyecdysone to epidermal growth factor receptor, fms-related receptor tyrosine kinase 1, and integrin subunit alpha 5, and molecular dynamics simulations supported the stability of these complexes. *In vitro* experiments showed that 20-hydroxyecdysone inhibited cell viability, clonogenicity, and migration, while promoting apoptosis. It also reduced the phosphorylation levels of phosphatidylinositol 3-kinase, protein kinase B, and glycogen synthase kinase 3 beta at Ser9 without markedly altering total protein expression. **Conclusion:** Treatment with 20-Hydroxyecdysone showed anti-glioma activity *in vitro* and may exert its effects, at least in part, through suppression of the phosphatidylinositol 3-kinase/protein kinase B signaling pathway. These findings support its further evaluation as a potential therapeutic candidate for glioblastoma.

**Keywords:** glioblastoma; phytochemicals; cell proliferation; apoptosis; PI3K/AKT signaling pathway

## 1. Introduction

Glioblastoma (GBM) is one of the most common and aggressive primary tumors of the central nervous system in adults. According to the latest Central Brain Tumor Registry of the United States (CBTRUS) statistics, GBM is the most frequent histologic subtype among malignant brain and central nervous system tumors, accounting for the largest proportion of malignant cases [1]. In the 2021 WHO classification of central nervous system tumors, glioblastoma (IDH-wildtype) is categorized as central nervous system (CNS) WHO grade 4, which underscores its highly invasive nature and highlights the importance of molecular subtyping in diagnosis and prognostic assessment [2]. Although surgical, radiotherapeutic, and chemotherapeutic strategies have continued to improve in recent years, overall outcomes for GBM remain limited. Standard treatment still centers on maximal safe resection followed by radiotherapy with concurrent and adjuvant temozolomide (TMZ), yet landmark randomized controlled trials showed that median overall survival remains only about 14.6 months [3]. More importantly, relapse or progression is almost inevitable, and no universally accepted standard therapy has yet been established for recurrent GBM. Current clinical strategies are therefore aimed mainly at achieving remission or delaying progression [4].

From a biological standpoint, the refractory nature of GBM largely reflects its marked heterogeneity and the dynamic interactions within the tumor microenvironment. Malignant features such as unchecked proliferation, eva-

sion of apoptosis, migration/invasion, and therapeutic resistance are usually driven by multiple pathways and display substantial network robustness [5]. For this reason, single-target interventions in a complex tumor such as GBM often face unstable efficacy and adaptive compensation. There is a clear need to identify candidate strategies better aligned with the multitarget, multipathway nature of the disease. Natural products and their derivatives have long served as an important source of antitumor agents and offer lead compounds with structural diversity and network-regulatory potential [6]. Consistent with this concept, network pharmacology examines drug–target–pathway–disease relationships from a systems and network biology perspective, providing a methodological basis for studying the multitarget mechanisms of natural products and identifying candidate molecules [7,8,9].

In drug discovery, reverse network pharmacology complements conventional compound-centered mechanism mining by reasoning backward from disease networks to candidate molecules. This approach first integrates disease-related genes and proteins, constructs interaction networks to identify key targets and core pathways, and then uses compound–target interaction databases for reverse matching to screen compounds capable of covering those key targets. Databases such as BATMAN-TCM 2.0 provide bidirectional retrieval and analysis, linking compounds to targets and targets or signature genes back to compounds, thereby offering both the data foundation and computational entry point for this type of reverse screening [10]. Within this framework, we identified 20-hydroxyecdysone (20E) as a potential candidate molecule. Importantly, 20E was prioritized not solely according to computational output, but based on an integrated consideration of target relevance, reported mammalian safety, experimental feasibility, and its relatively limited investigation in GBM compared with several other candidate natural compounds. Previous reviews have shown that 20E has low mammalian toxicity and broad biological activity [11]. In several tumor models, 20E has been associated with antitumor phenotypes or transcriptomic changes and has been reported to inhibit proliferation, induce apoptosis, or suppress migration and invasion [12,13]. In addition, the ability of ecdysteroids and their derivatives to sensitize multidrug-resistant models to chemotherapy further suggests potential value in combination treatment settings [14].

At the mechanistic level, the PI3K/AKT/GSK3β axis is a major signaling axis in GBM and is closely associated with cell proliferation, survival, migration/invasion, and treatment resistance. It also has strong biological interpretability and translational relevance in cancer therapeutics [15,16]. Accordingly, this study used reverse network pharmacology as the main strategy to systematically identify the key target network of GBM and to reversely screen candidate natural active compounds. After prioritizing 20E, we proposed testable pathway hypotheses through molecular docking and then validated them in U87 and U251 glioma cells, with SVG p12 cells as controls, by combining phenotypic assays of cell viability (CCK-8), colony formation, apoptosis-associated changes, and migration with AKT-related protein detection. In this way, we sought to establish an evidence chain linking reverse screening, mechanistic anchoring, and experimental validation.

## 2. Materials and Methods

### *2.1 Glioblastoma Target Collection*

Glioblastoma-related targets were retrieved from GeneCards (https://www.genecards.org/) and DisGeNET (https://www.disgenet.org/) using "glioblastoma" as the search term. For GeneCards, the top 25% of targets ranked by score were retained, whereas for DisGeNET, targets with a score ≥0.7 were selected. The GSE2223 series (normal, n = 4; GBM, n = 27) was downloaded from the GEO database (https://www.ncbi.nlm.nih.gov/gds/) and analyzed using GEO2R. Targets with |log2FC| >1.5 were selected. After standardization through UniProt (https://www.uniprot.org/), the targets obtained from the two databases were deduplicated and integrated. Intersections with the differentially expressed genes were identified using Venny 2.1.0 (BioinfoGP, Spanish National Biotechnology Centre, CNB-CSIC, Madrid, Spain; RRID: SCR_016561), yielding 136 GBM-related disease targets.

### *2.2 PPI Network Construction and Core Target Screening*

The 136 GBM-related targets were imported into the STRING database (https://cn.string-db.org/) to construct a protein-protein interaction network, using the highest confidence level (>0.9). The network file was then exported and imported into Cytoscape version 3.10.4 (Cytoscape Consortium, San Diego, CA, USA). Four CytoHubba topological algorithms-maximal clique centrality (MCC), maximum neighborhood component (MNC), edge percolated component (EPC), and Degree-were used to rank potential hub targets. Intersection analysis of the top-ranked results identified 18 core targets.

### *2.3 Enrichment Analysis and Disease–Target–Drug Network Construction*

The 136 disease targets were subjected to Gene Ontology (GO) and Kyoto Encyclopedia of Genes and Genomes (KEGG) enrichment analyses using the DAVID database (https://davidbioinformatics.nih.gov/). The results were visualized on the MicroBioInformatics platform (https://www.bioinformatics.com.cn/). For GO visualization, terms with $p < 0.01$ and false discovery rate (FDR) <0.01 were retained. The 18 core targets were then imported into BATMAN-TCM 2.0 (http://bionet.ncpsb.org.cn/batman-tcm/#/home) for component matching, and Cytoscape (version 3.10.4) was used to visualize the relationships among diseases, targets, and drug components.

*2.4 Molecular Docking and Molecular Dynamics Simulation*

Candidate drug components identified through reverse screening and their corresponding targets were first determined. The phosphoinositide 3-kinase (PI3K)-protein kinase B (AKT) signaling pathway, which contained both enriched targets and matched candidate compounds, was selected for subsequent analysis. Molecular docking was then performed between the candidate compounds and proteins enriched in this pathway. The three-dimensional structures of the compounds were downloaded from ChemSpider (https://www.chemspider.com/). Protein accession information was obtained from UniProt, and receptor structures containing standard ligands were downloaded from the PDB database (https://www.rcsb.org/). Receptor and ligand preprocessing, including dehydration, hydrogenation, and charge assignment, was performed using PyMOL version 3.0.3 (Schrödinger, LLC, New York, NY, USA) and AutoDockTools version 1.5.6 (Molecular Graphics Laboratory, The Scripps Research Institute, La Jolla, CA, USA). Docking grids were defined according to the standard ligand-binding sites, and docking was carried out using AutoDock Vina. Binding modes and minimum binding energies were analyzed. Molecular dynamics simulations were subsequently performed for proteins showing lower minimum binding energies in complex with the candidate compounds.

*2.5 Cell Culture*

The human glial cell line SVG p12 and the glioma cell lines U87 and U251 were purchased from Hunan Fenghui Biotechnology Co., Ltd. Cells were maintained in high-glucose DMEM (Gibco, 12100046) supplemented with 10% fetal bovine serum (FBS; Gibco, A5256701) at 37 °C in a humidified incubator with 5% $CO_2$.

All cell lines used in this study were validated by STR profiling and tested negative for mycoplasma contamination.

2.5.1 Cell Recovery

Cells stored in liquid nitrogen were removed and thawed in a 37 °C water bath within 2 min. The cell suspension was transferred to a 15-mL centrifuge tube, mixed with 4 mL of complete medium, and centrifuged at 1000 rpm for 5 min. The supernatant was discarded, and the cells were resuspended in 4 mL of complete medium containing 10% serum. The suspension was then transferred to a T25 culture flask and gently agitated to distribute the cells evenly across the bottom of the flask. The recovery date, operator, and passage number were recorded. Cells were cultured at 37 °C in 5% $CO_2$.

2.5.2 Cell Passaging

Cells were passaged when they reached approximately 90% confluence. All procedures were performed in a biosafety cabinet. Cells were washed three times with sterile PBS from the cell-free side of the flask, after which 1 mL of 0.25% trypsin was added for digestion. Cells were monitored under a microscope until they became round, bright, and slightly contracted. The bottom of the flask was gently tapped until a large proportion of the cells detached, and complete medium was immediately added to stop digestion. An additional 3 mL of PBS was used to rinse the flask, and the cell suspension was collected into a centrifuge tube and centrifuged at 1000 rpm for 3 min. After discarding the supernatant, 2 mL of complete medium was added to resuspend the cells evenly, and an appropriate volume was seeded into a new T25 flask for continued culture at 37 °C and 5% $CO_2$.

2.5.3 Cell Cryopreservation

Cells were collected using the same procedure as for passaging. After centrifugation, the supernatant was removed, an appropriate volume of cryopreservation medium was added, and the cells were gently resuspended. The suspension was transferred to cryovials, placed in a programmed freezing box at −80 °C for 24 h, and then moved to liquid nitrogen for long-term storage.

*2.6 CCK-8 Assay*

U251, U87, and SVG p12 cells in logarithmic growth were seeded into 96-well plates at a density of $3 \times 10^3$ cells/well. PBS was added to the peripheral wells to minimize edge effects. Cells were incubated at 37 °C with 5% $CO_2$ for 24, 48, and 72 h. The cells were divided into a blank group, a 0 mM vehicle control group, and 20E-treated groups receiving 0.04, 0.08, 0.12, 0.16, or 0.20 mM 20-hydroxyecdysone (20E; Cat. No. H408562, Shanghai Aladdin Biochemical Technology Co., Ltd., Shanghai, China). The stock solution was stored at −80 °C and diluted in 2% DMEM to the desired concentrations. The blank group received 100 µL of 2% DMEM, the 0 mM vehicle control group received 100 µL of 2% DMEM containing the same volume of DMSO as the 20E-treated groups, and the treatment groups received 100 µL of 2% DMEM containing the indicated 20E concentrations. After incubation for 24, 48, or 72 h, cells were washed twice with sterile PBS. Each well was then incubated with 100 µL of basal medium containing 10% Cell Counting Kit-8 solution (CCK-8; Cat. No. abs50003, Absin Bioscience Inc., Shanghai, China) in the dark at 37 °C for approximately 1 h, and absorbance was measured at 450 nm.

*2.7 Colony Formation Assay*

U251 and U87 cells in logarithmic growth were digested with trypsin to generate single-cell suspensions and counted. Cells were seeded into 6-well plates at a density of 1000 cells/well. After attachment, the cells were treated with 0, 0.04, 0.08, 0.12, 0.16, or 0.20 mM 20E and cultured for 14 days. The 0 mM group received the same volume

of DMSO and served as the vehicle control. When visible colonies had formed, the medium was discarded and the cells were gently washed twice with prechilled PBS. Cells were fixed with 4% paraformaldehyde for 30 min, stained with 1 mL of 0.1% crystal violet for 40 min, and then washed with running water to remove excess dye. The plates were air-dried and photographed.

*2.8 Wound-Healing Assay*

U251 and U87 cells in logarithmic growth were digested with trypsin, resuspended in DMEM containing 10% fetal bovine serum, and seeded into 6-well plates at a density of $3 \times 10^4$ cells/well. Cells were cultured at 37 °C in 5% $CO_2$ until they reached 90%–100% confluence and formed a monolayer. Using a sterile 200-µL pipette tip held perpendicular to the well and the premarked guide line, a straight scratch was made rapidly and evenly across the monolayer. The same pressure was used throughout to maintain a consistent scratch width. After scratching, the medium was carefully aspirated and the cells were gently rinsed two to three times with sterile PBS to remove detached cells. Serum-free or low-serum maintenance medium (e.g., 1% serum) was then added, and the cells were returned to the incubator. Cell migration was observed under an inverted microscope at 0, 12, 24, and 36 h after scratching for U87 cells and at 0, 24, 36, and 48 h after scratching for U251 cells. Images were captured at the same scratch location at each time point. Alignment marks were drawn on the underside of the plate to ensure consistent imaging. Scratch area or width was quantified using image-analysis software such as ImageJ version 2.3.0 (National Institutes of Health, Bethesda, MD, USA).

*2.9 Apoptosis Assay*

For TUNEL staining, U251 cells were treated with the indicated concentrations of 20E for 24 h, fixed with 4% paraformaldehyde for 30 min, washed twice with 1× PBS for 5 min each, and residual PBS was removed with absorbent paper. Permeabilization buffer was added for 5 min, followed by two further PBS washes. A total of 100 µL of 1× Equilibration Buffer (APExBIO, K1133) was added to each sample to fully cover the sample area, and equilibration was carried out at room temperature for 10 min. After equilibration, 50 µL of reaction solution was added and incubation was performed at 37 °C for 1 h. The samples were then washed twice with PBS, nuclear dye was added, and the slides were mounted. TUNEL-positive cells were observed under a fluorescence microscope.

Annexin V-FITC/PI double staining (Elabscience, E-CK-A211) was used to assess apoptosis-associated cell populations in U87 cells. Cells in logarithmic growth were seeded into 6-well plates and treated with the indicated 20E concentrations for 24 h. Cells from each well were collected together with the culture medium. Adherent cells were then detached using EDTA-free trypsin, and digestion was stopped with the previously collected medium. The cell suspension was centrifuged at 1000 rpm for 5 min, washed once with prechilled PBS, and resuspended in 100 µL of 1× binding buffer at a density of approximately $1 \times 10^5$–$1 \times 10^6$ cells/mL. Annexin V-FITC (5 µL) and PI staining solution (5 µL) were added sequentially, and the cells were incubated for 15 min at room temperature in the dark. After incubation, 400 µL of 1× binding buffer was added to each tube and flow cytometry was performed immediately. Flow cytometry data were analyzed using FlowJo version 10.8.1 (FlowJo, LLC, Ashland, OR, USA). Cellular events were first gated according to forward-scatter area and side-scatter area characteristics to exclude debris. Singlet events were then selected based on forward-scatter pulse geometry to exclude doublets and cell aggregates. Annexin V-FITC/PI quadrant boundaries were established using an unstained blank control and single-stained Annexin V-FITC and PI controls. The same sequential gating strategy and quadrant settings were applied consistently to all vehicle- and 20E-treated samples within each independent experiment. Q4 represented viable cells (Annexin V-FITC−/PI−), Q3 represented early apoptotic cells (Annexin V-FITC+/PI−), Q2 represented late apoptotic or secondary necrotic cells (Annexin V-FITC+/PI+), and Q1 represented primarily necrotic cells (Annexin V-FITC−/PI+). The total apoptotic rate was calculated as the sum of Q2 and Q3. The experiment was performed using three independent biological replicates (n = 3).

*2.10 Western Blotting*

U251 and U87 cells were seeded into T25 culture flasks. When cell density reached approximately 50%–60%, the cells were treated with 0 or 0.12 mM 20E for 24 h. The 0 mM group received the same volume of DMSO and served as the vehicle control; therefore, it represented the DMSO solvent control for Western blotting. The 0.12 mM concentration was selected as a representative mechanistic condition because it produced clear phenotypic effects without causing excessive cell loss in preliminary viability and morphological observations. Cells were then collected and lysed on ice for 30 min using 200 µL of lysis buffer prepared as RIPA:PMSF:phosphatase inhibitor = 99:1:1. After scraping, samples were centrifuged at 12,000 rpm for 15 min at 4 °C, and the supernatants were collected for Western blot analysis. Protein concentrations were measured using a BCA protein assay kit. Protein samples were adjusted to equal concentrations and volumes, mixed with 5× loading buffer, heated at 100 °C for 10 min to denature the proteins, cooled, and briefly centrifuged before use. After electrophoresis, membrane transfer, and blocking, membranes were incubated overnight at 4 °C with the following primary antibodies: GAPDH (1:10,000, Cat. No. AF7021, Affinity Biosciences, Cincinnati, OH, USA), phospho-AKT (Ser473) (D9E) rabbit monoclonal antibody (1:2000, Cat. No. 4060,

Cell Signaling Technology, Danvers, MA, USA), AKT (CST, C67E7, 1:1000), Phospho-PI3K antibody (1:1000, Cat. No. 341468, Zen Bioscience, Chengdu, Sichuan, China), PI3K (Zenbio, R22768, 1:10,000), GSK3β (CST, D5C5Z, 1:1000), and p-GSK3β (Ser9) (CST, D85E12, 1:1000). On the following day, membranes were washed three times with TBST for 5 min each and then incubated with HRP-conjugated secondary antibody (Cat. No. 31460, Lot No. XK368089, Thermo Fisher Scientific, Waltham, MA, USA) at room temperature for 2 h, followed by three additional TBST washes. Super ECL Detection Reagent (Cat. No. 36208ES76, Yeasen Biotechnology (Shanghai) Co., Ltd., Shanghai, China) was added for 1 min at room temperature, and bands were visualized using a chemiluminescence imaging system. ImageJ was used to quantify band intensity, and relative protein expression was expressed as the ratio of the target protein band intensity to that of the corresponding loading or total protein control.

### *2.11 Statistical Analysis*

All data were analyzed using GraphPad Prism 10.1.2 (GraphPad Software, LLC, Boston, MA, USA). Results are presented as the mean ± standard deviation (SD). Differences between two groups were assessed using the paired Student's *t*-test when samples were generated as matched pairs within the same independent experiment. Specifically, in each independent biological replicate, cells from the same batch were divided into Vehicle and drug groups and processed in parallel. For comparisons among multiple treatment groups, one-way ANOVA followed by Dunnett's multiple comparisons test was used to compare each treatment group with the 0 mM vehicle control group. $p$ value $< 0.05$ was considered statistically significant.

## 3. Results

### *3.1 Identification of Disease Targets and Intersecting Targets*

Searching the GeneCards and DisGeNET databases yielded a total of 2422 glioblastoma-related targets. At the same time, differential expression analysis of the GEO dataset GSE2223 identified 840 differentially expressed genes between GBM and normal brain tissue (Fig. 1A). Intersecting the disease-related target set with the differentially expressed gene set yielded 136 shared targets (Fig. 1B). Of these, 704 genes were specific to GSE2223, whereas 2286 were specific to GeneCards and DisGeNET. These 136 intersecting targets were used for subsequent protein–protein interaction (PPI) network construction, hub-gene screening, and enrichment analysis.

### *3.2 PPI Network Analysis and Identification of Core Targets*

The 136 intersecting targets were imported into a PPI platform to construct a protein interaction network (Fig. 1C). The resulting network showed highly connected modules and dense interaction patterns, suggesting that these targets may act cooperatively in key pathological processes associated with GBM. To identify hub nodes, four CytoHubba algorithms-MCC, MNC, EPC, and Degree-were applied to the network, and the common intersection of the four ranking methods was defined as the core target set. This analysis consistently identified 18 core targets (Fig. 1D,E): EGFR, ESR1, CD4, CD44, CASP3, CTLA4, PXDN, LYN, CD86, FLT1, TGFBR1, JAG1, SOCS3, BCL6, SERPINE1, CHEK1, PXN, and THY1. The high-ranking node networks generated by the four algorithms are shown in Fig. 1F, where node color intensity and size reflect network centrality, further supporting the key role of these targets in GBM-related networks.

### *3.3 GO and KEGG Analyses*

GO enrichment analysis was performed on the 136 intersecting targets. After filtering by $p$ value and FDR, 26 biological process (BP) terms, 16 cellular component (CC) terms, and 14 molecular function (MF) terms were obtained (Fig. 2A). The BP terms were mainly associated with signal transduction, cell adhesion and intracellular signal transduction, angiogenesis, regulation of apoptosis, regulation of cell population proliferation, nervous system development, regulation of cell migration, and the DNA damage response. The CC terms were mainly enriched in membrane/plasma membrane, cytoplasm/cytosol, nucleoplasm, extracellular exosomes, cell surface, synapses, and focal adhesions. The MF terms were primarily related to protein binding, nucleotide/ATP binding, protein kinase activity, calcium ion binding, signal receptor binding, and serine/threonine protein kinase activity. Overall, these intersecting targets were closely associated with key signaling, adhesion and migration, and cell-fate determination processes in GBM.

KEGG enrichment analysis (Fig. 2B) revealed significant enrichment of multiple tumor-related signaling modules. Based on the Sankey plot and bubble plot, 30 significantly enriched pathways were visualized, including pathways in cancer, proteoglycans in cancer, the MAPK signaling pathway, Ras/Rap1 signaling, ErbB signaling, HIF-1 signaling, focal adhesion, and microRNAs in cancer. Importantly, the PI3K/AKT signaling pathway was clearly represented among the enriched pathways and was connected to multiple genes in the Sankey diagram, suggesting that it may act as a major convergence module within the intersecting target network. The PI3K/AKT pathway was selected as the principal mechanistic anchor not merely because it appeared in the enrichment output, but because it was biologically relevant to the observed phenotypes of proliferation, survival, apoptosis, and migration, included upstream nodes suitable for structural analysis, and could be experimentally evaluated through phosphorylation-dependent pathway markers [17]. Considering these factors, we selected the PI3K/AKT signaling pathway for subsequent structural and cellular validation.

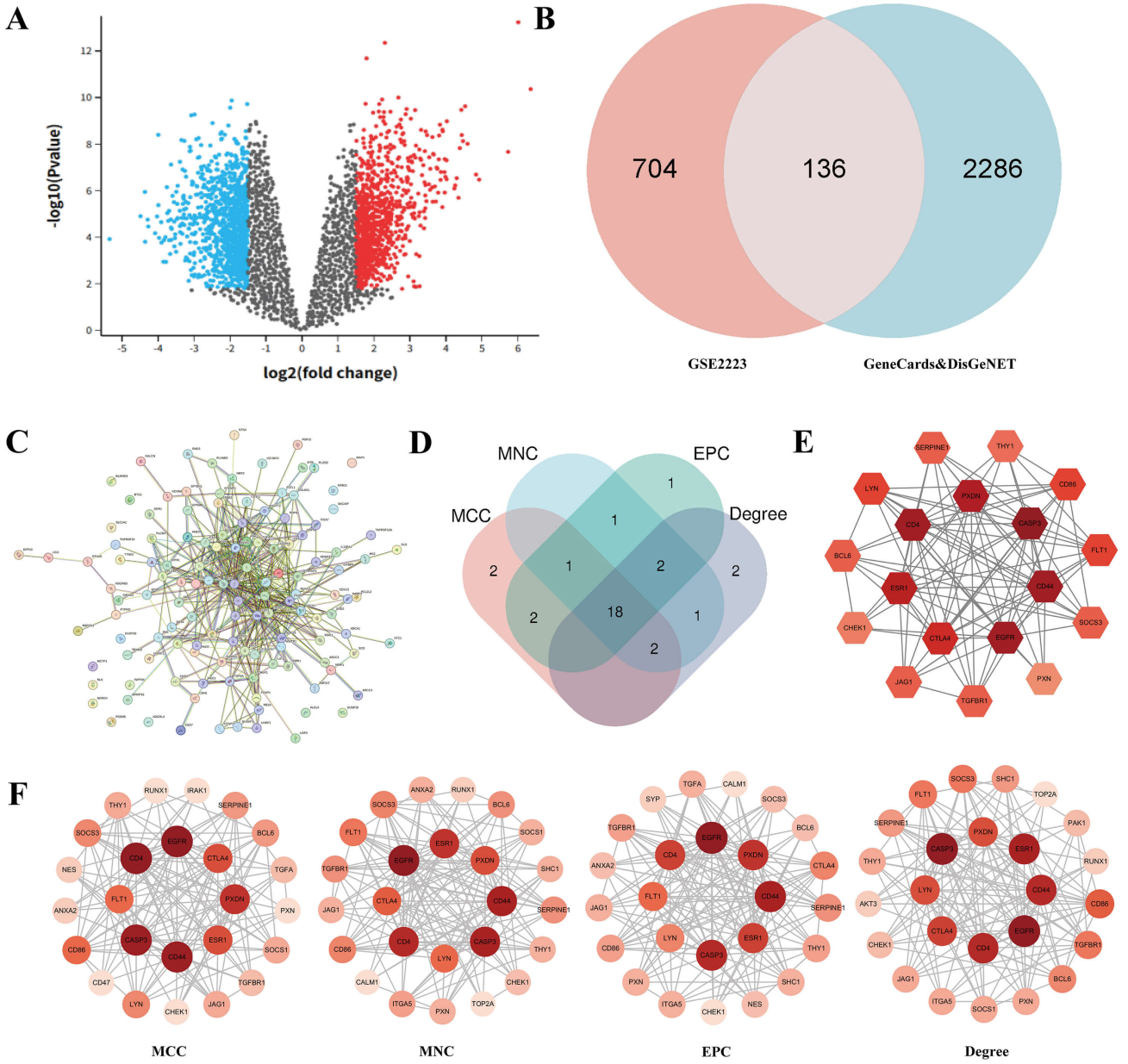


**Fig. 1. Identification of glioblastoma-related targets and hub genes**. (A) Volcano plot showing differentially expressed genes (DEGs) between glioblastoma and normal brain tissues in the GEO dataset (GSE2223). Red dots indicate upregulated genes and blue dots indicate downregulated genes, while gray dots represent genes without significant differential expression. (B) Venn diagram showing the overlap between glioblastoma (GBM)-related genes collected from GeneCards/DisGeNET and DEGs from GSE2223; 136 intersecting targets were identified for subsequent analyses. (C) Protein–protein interaction (PPI) network constructed using the 136 intersecting targets. (D) Venn diagram showing the intersection of hub genes ranked by four cytoHubba algorithms (maximal clique centrality [MCC], maximum neighborhood component [MNC], edge percolated component [EPC] and Degree); 18 common hub targets were obtained. (E) PPI subnetwork of the 18 common hub targets; node size/color indicate topological importance. (F) Top-ranked nodes identified by each cytoHubba algorithm (MCC, MNC, EPC and Degree), illustrating the robustness of hub selection across algorithms.

*3.4 Reverse Network Pharmacology*

The 18 core targets were imported into BATMAN-TCM 2.0 for compound matching and enrichment analysis, and a disease–target–compound/drug (and source) relationship network was constructed (Fig. 2C). The network showed clear one-to-many relationships between candidate compounds and core targets, suggesting that these molecules may exert network-level regulatory effects by covering multiple hub nodes. According to the BATMAN-TCM enrichment ranking, the main candidate compounds included peiminine, delphinidin chloride, alizarin 1-methyl ether, and 20E. Because the present study was designed as

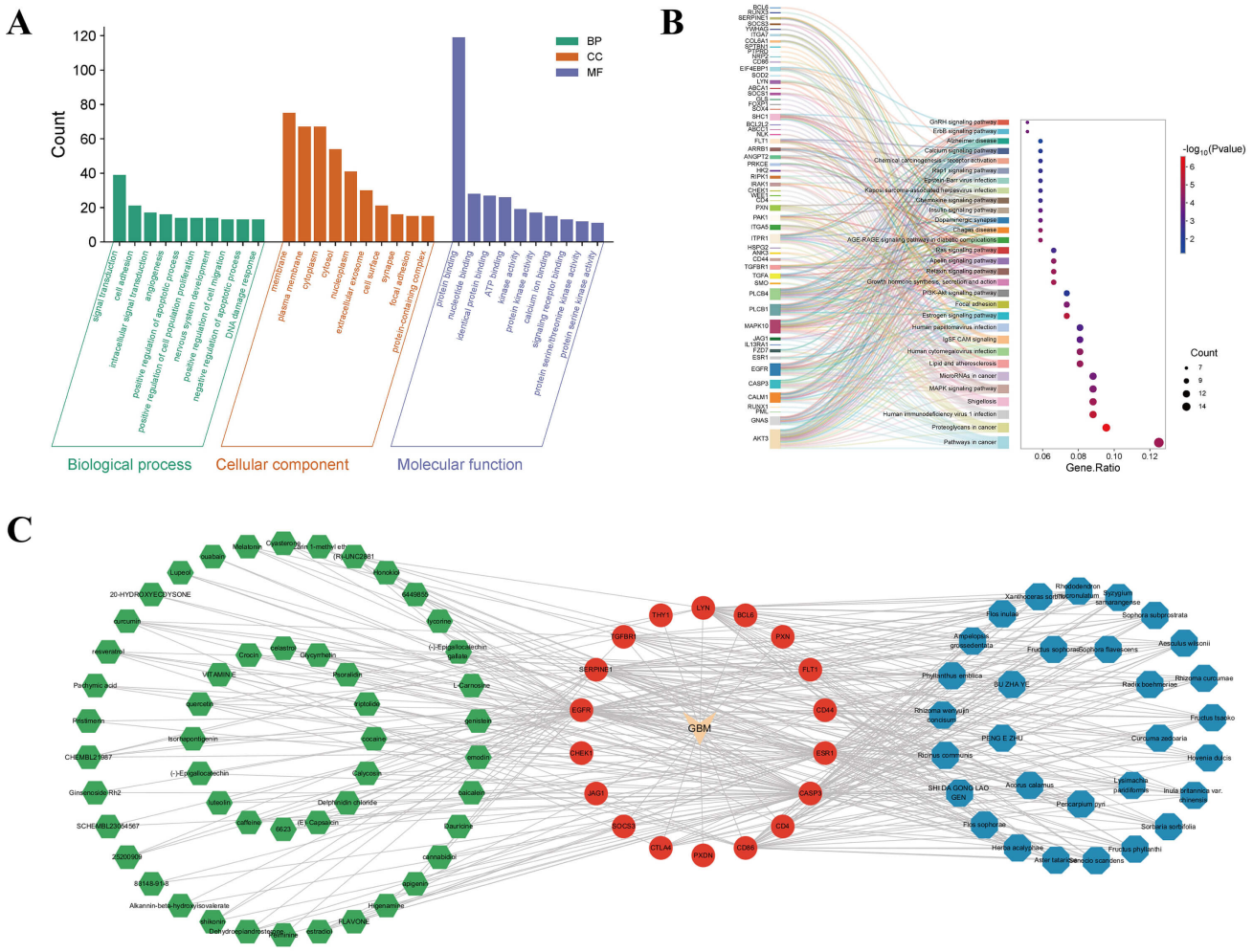


**Fig. 2. Functional enrichment analyses and reverse network pharmacology screening of candidate compounds**. (A) Gene Ontology (GO) enrichment results of the 136 intersecting targets, including biological process (BP), cellular component (CC) and molecular function (MF); representative top terms are shown. (B) KEGG pathway enrichment of intersecting targets visualized by an alluvial (Sankey) plot and bubble plot; pathway significance and gene ratios are indicated as shown. The PI3K/AKT signaling pathway was among the enriched pathways and was selected for downstream validation. (C) Disease–target–compound–herb network constructed based on BATMAN-TCM 2.0 reverse screening using hub targets. Green nodes represent candidate compounds, red nodes represent targets, blue nodes represent herbs, and the central node indicates glioblastoma; 20-hydroxyecdysone was identified as a prioritized candidate compound. KEGG, Kyoto Encyclopedia of Genes and Genomes; PI3K, phosphoinositide 3-kinase; AKT, protein kinase B.

an initial proof-of-concept validation rather than a head-to-head comparison of all candidate compounds, one representative compound was selected for downstream experimental validation. Previous studies have shown that peiminine inhibits glioblastoma proliferation and slows tumor progression *in vitro* and *in vivo* [18], whereas delphinidin-related compounds have been reported to reduce glioma cell viability or alleviate temozolomide resistance [19]. Therefore, to avoid simply repeating previously investigated glioma-related natural compounds, these compounds were not prioritized in the present study. Among the remaining candidates, 20E was selected as a representative compound because it has a relatively well-documented mammalian pharmacological and safety background, available human safety/pharmacokinetic data, and prior *in vitro* cancer-cell evidence supporting feasible downstream experimental validation [20,21]. Importantly, alizarin 1-methyl ether was not excluded because of limited evidence or presumed toxicity; rather, it remains another candidate compound that requires independent computational and experimental evaluation. Therefore, the present study should be interpreted as an initial validation of 20E as one representative candidate, not as evidence that 20E is superior to all other compounds identified by reverse screening.

**Table 1. Molecular docking binding energies of 20-hydroxyecdysone with PI3K/AKT pathway-related targets.**

| | Molecular docking binding energies (unit: kcal/mol) |
|---|---|
| AKT3-20-hydroxyecdysone | –5.9 |
| ANGPT2-20-hydroxyecdysone | –5.9 |
| COL6A1-20-hydroxyecdysone | –6.4 |
| EGFR-20-hydroxyecdysone | –8.1 |
| EIF4EBP1-20-hydroxyecdysone | –3.9 |
| FLT1-20-hydroxyecdysone | –7.9 |
| ITGA5-20-hydroxyecdysone | –7.6 |
| ITGA7-20-hydroxyecdysone | –6.1 |
| TGFA-20-hydroxyecdysone | –4.9 |
| YWHAG-20-hydroxyecdysone | –5.5 |

### *3.5 Molecular Docking and Molecular Dynamics Simulations*

To investigate the potential interactions between 20-hydroxyecdysone and PI3K/AKT pathway-related targets, molecular docking was carried out for 10 proteins identified from the pathway enrichment analysis. The docking scores ranged from −3.9 to −8.1 kcal/mol (Table 1), indicating different levels of binding affinity among the targets. Among them, EGFR, FLT1, and ITGA5 showed relatively stronger binding and were therefore selected for subsequent structural and dynamic analyses.

Examination of the docking conformations indicated that 20-hydroxyecdysone could be accommodated within the binding pockets of FLT1, EGFR, and ITGA5, where it formed multiple hydrogen-bonding and hydrophobic contacts with surrounding residues. In the FLT1 complex, the main interacting residues included ASN39, LEU42, ARG72, and PHE133. In the EGFR complex, the ligand mainly interacted with THR766, MET769, CYS773, and ARG817. In the ITGA5 complex, the principal interacting residues were ARG106, PHE168, LEU355, SER417, LEU419, VAL235, and VAL289. The interaction distances were mainly distributed between 2.8 and 3.3 Å, supporting favorable ligand accommodation within these binding sites (Fig. 3A).

Based on these docking results, 100-ns molecular dynamics simulations were performed for the three selected complexes to further evaluate their dynamic behavior. The RMSD profiles showed that all three systems remained generally stable during the simulation, with fluctuations within approximately 0.3 nm (Fig. 3B). The RMSF analysis showed relatively low residue fluctuations overall, except for a few flexible regions, indicating that ligand binding did not induce marked structural instability (Fig. 3C). Intermolecular hydrogen bonds were maintained throughout the simulations, with the FLT1–20-hydroxyecdysone complex showing the highest hydrogen-bond occupancy (Fig. 3D). The radius of gyration (Rg) also remained stable, fluctuating within 2.16–2.20 nm for ITGA5, 1.95–2.00 nm for EGFR, and 1.56–1.62 nm for FLT1, indicating that the overall compactness of the three complexes was well preserved during the simulation (Fig. 3E). Together, these results support the stable association of 20-hydroxyecdysone with the selected PI3K/AKT pathway-related targets.

### *3.6 20-Hydroxyecdysone Affects Glioma Cell Viability and Morphology*

To evaluate the effect of 20-hydroxyecdysone (20E) on glioma cell proliferation, U251 and U87 cells were used as tumor cell models, and SVG p12 cells were used as a control cell line. Cells were treated with 0, 0.04, 0.08, 0.12, 0.16, or 0.20 mM 20E, with the 0 mM group receiving the same volume of DMSO as the vehicle control. CCK-8 assays were performed at 24, 48, and 72 h, and each concentration was compared with the corresponding 0 mM vehicle control within the same cell line and time point.

In U251 cells, 20E reduced cell viability, particularly at medium-to-high concentrations and longer treatment durations. At 24 h, significant inhibition was observed at 0.12 and 0.20 mM, with viability reduced to 84.8% and 87.0% of the 0 mM vehicle control, respectively. At 48 h, the inhibitory effect became more evident, with viability reduced to 75.2%, 56.6%, 51.7%, and 42.0% of control at 0.08, 0.12, 0.16, and 0.20 mM, respectively. At 72 h, 0.12–0.20 mM 20E further reduced U251 cell viability to 76.8%, 44.3%, and 31.2% of control, respectively (Fig. 4A–C).

In U87 cells, low-dose exposure produced modest fluctuations at selected time points, whereas increasing concentration and longer treatment generally reduced viability. Specifically, 0.08 mM 20E increased U87 cell viability to 120.7% of control at 24 h, and 0.04 mM increased viability to 116.3% of control at 72 h. However, this low-dose increase was not sustained across higher concentrations. At 48 h, 0.04–0.20 mM 20E significantly reduced cell viability to 92.2%, 75.3%, 60.0%, 54.0%, and 45.3% of the control, respectively. At 72 h, 0.08–0.20 mM 20E reduced viability to 86.3%, 52.3%, 57.6%, and 42.7% of control, respectively (Fig. 4D–F).

In SVG p12 control cells, viability remained largely stable at low-to-medium concentrations. Significant inhibitory effects were mainly observed under higher-dose and/or longer-exposure conditions. Specifically, SVG p12

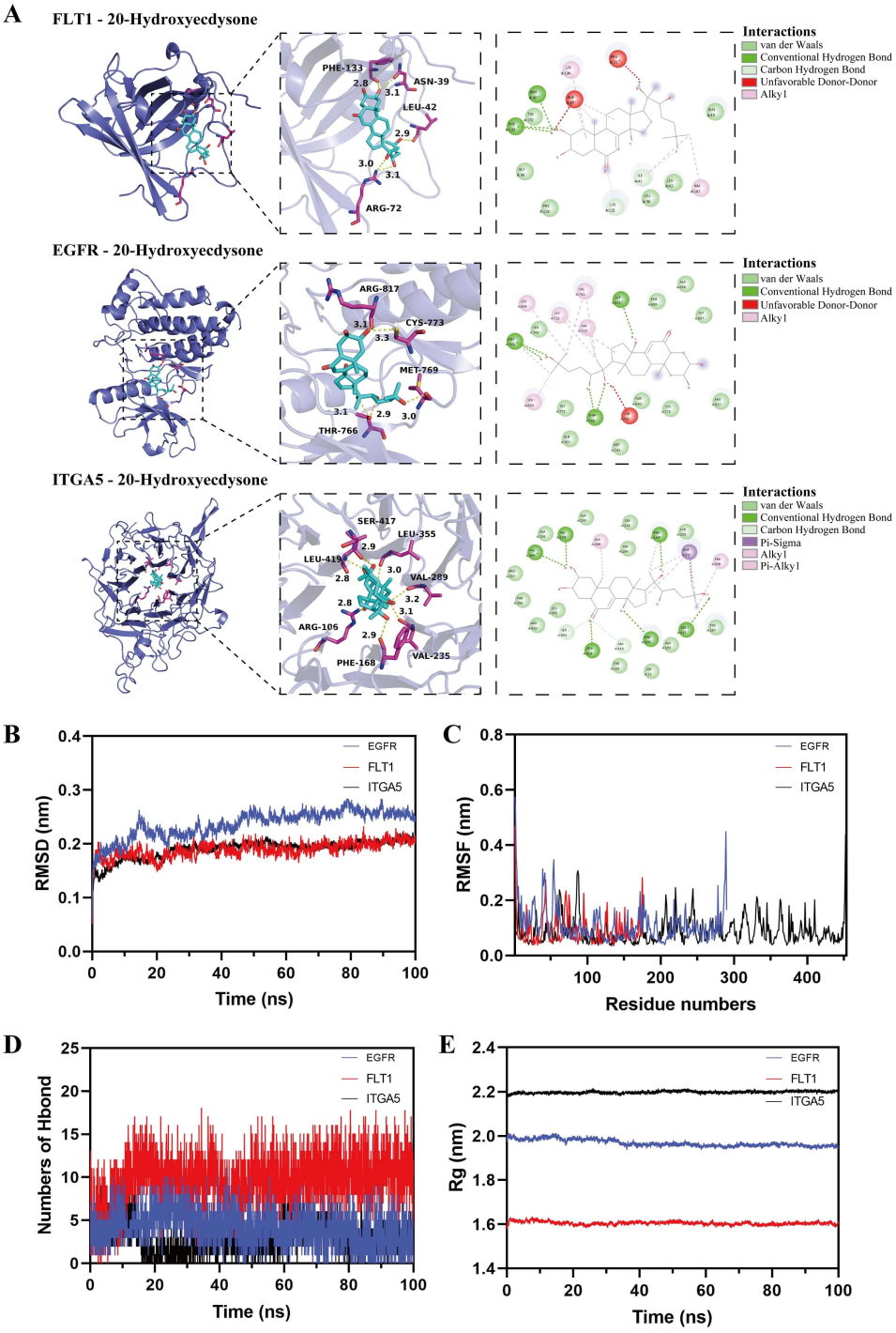


**Fig. 3. Molecular docking and molecular dynamics simulations based on PI3K/AKT pathway–enriched targets**. (A) Representative docking poses of 20-hydroxyecdysone with key PI3K/AKT pathway–related proteins (e.g., FLT1, EGFR and ITGA5), with corresponding 2D interaction diagrams showing hydrogen bonds and hydrophobic contacts. (B–E) Molecular dynamics simulations (100 ns) for selected complexes. (B) RMSD curves of protein–ligand complexes. (C) RMSF profiles of protein residues. (D) Time evolution of hydrogen bond numbers between ligand and protein. (E) Radius of gyration (Rg) of complexes, indicating overall compactness during simulation. RMSD, root mean square deviation; RMSF, root mean square fluctuation.

viability was reduced to 91.0% of control at 0.20 mM for 24 h, to 96.0% and 89.7% of control at 0.16 and 0.20 mM for 48 h, and to 65.8% of control at 0.20 mM for 72 h (Fig. 4G–I). These data suggest that 20E showed stronger growth-inhibitory effects in glioma cells than in SVG p12 control cells within most of the tested range, although control cells were also affected under high-exposure conditions.

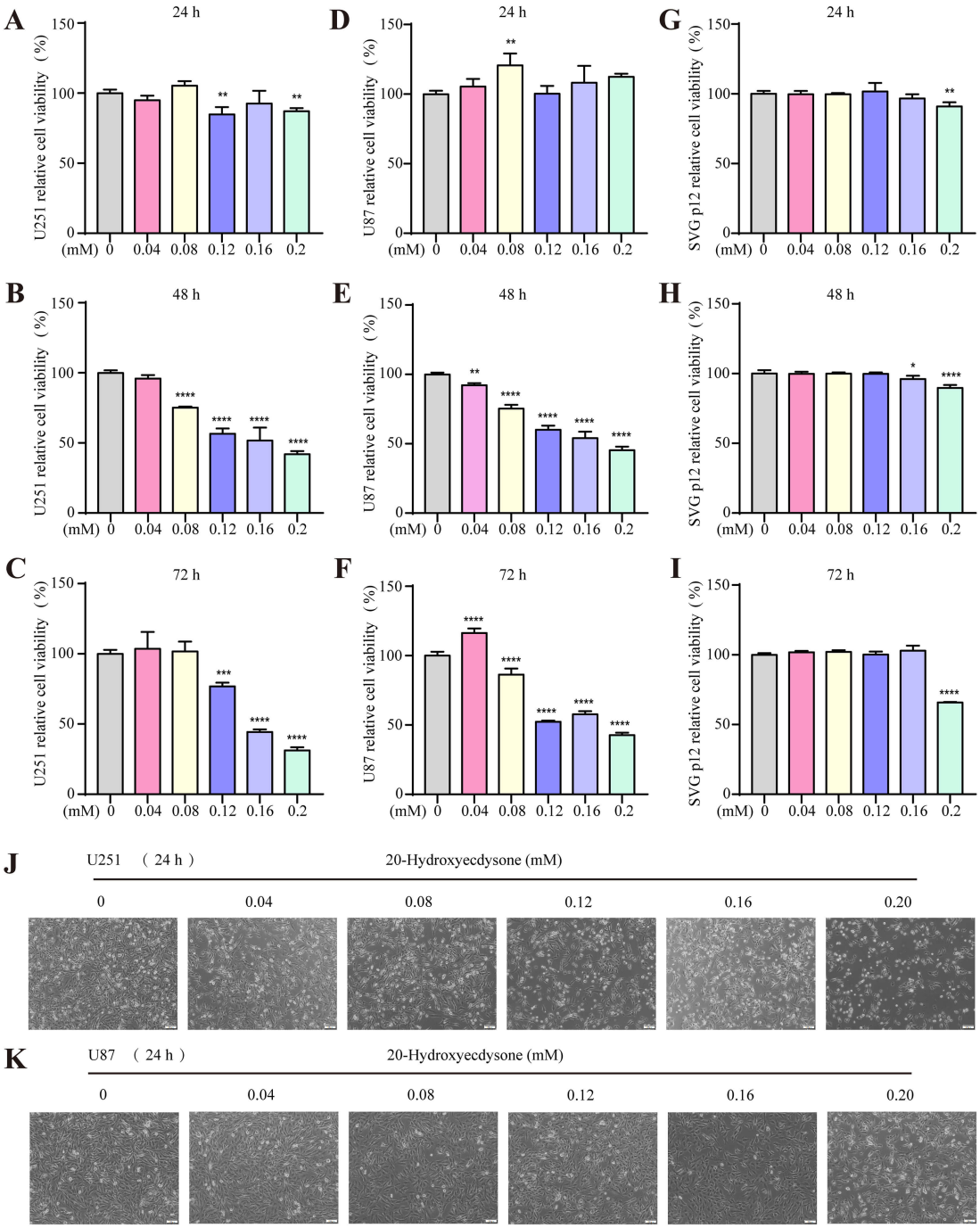


**Fig. 4. Effects of 20-hydroxyecdysone on glioblastoma and control cell viability and morphology**. (A–C) CCK-8 analysis of U251 cell viability after treatment with 0, 0.04, 0.08, 0.12, 0.16, or 0.20 mM 20-hydroxyecdysone for 24 h, 48 h, and 72 h, respectively. (D–F) CCK-8 analysis of U87 cell viability after treatment with the indicated concentrations of 20-hydroxyecdysone for 24 h, 48 h, and 72 h, respectively. (G–I) CCK-8 analysis of SVG p12 control cell viability after treatment with the indicated concentrations of 20-hydroxyecdysone for 24 h, 48 h, and 72 h, respectively. (J,K) Representative phase-contrast images of U251 and U87 cells after treatment with 0–0.20 mM 20-hydroxyecdysone for 24 h. The 0 mM group was treated with the same volume of DMSO and served as the vehicle control. Scale bar = 100 μm. Data are presented as the mean ± standard deviation (SD) from four independent technical replicates (n = 4). For comparisons among multiple treatment groups, statistical significance was analyzed using one-way ANOVA followed by Dunnett's multiple comparisons test versus the 0 mM vehicle control group. *$p < 0.05$; **$p < 0.01$; ***$p < 0.001$; ****$p < 0.0001$. CCK-8, Cell Counting Kit-8.

Representative phase-contrast images captured after 24 h showed that 20E treatment reduced cell density and induced visible morphological alterations in U251 and U87 cells, especially at higher concentrations (Fig. 4J,K). These results indicate that 20E suppresses glioblastoma cell growth, while its effects differ depending on cell line, concentration, and treatment duration.

### *3.7 20-Hydroxyecdysone Is Associated With Apoptosis-Related Changes in Glioma Cells*

To determine whether 20E-mediated growth inhibition was accompanied by increased apoptosis-associated cell death, we repeated the Annexin V-FITC/PI flow cytometry assay in U87 cells using standardized cross-gating and performed quantitative analysis based on three independent biological replicates. The total apoptotic population was defined as the sum of Q2 and Q3. Quantitative analysis showed that the total apoptotic rate was 18.02 ± 1.63% in the 0 mM vehicle control group and 17.53 ± 3.49%, 24.50 ± 8.58%, 46.49 ± 0.44%, 44.36 ± 1.09%, and 50.64 ± 2.26% after treatment with 0.04, 0.08, 0.12, 0.16, and 0.20 mM 20E, respectively. Compared with the 0 mM vehicle control group, 20E significantly increased the total apoptotic population at 0.12, 0.16, and 0.20 mM, whereas no significant difference was observed at 0.04 or 0.08 mM (Fig. 5A,B).

To further examine apoptotic DNA fragmentation, TUNEL staining was performed in U251 cells. Representative fluorescence images showed increased TUNEL-positive signals after 20E treatment. Quantification of relative TUNEL intensity showed significant increases at selected concentrations, reaching 1.07-fold, 1.12-fold, and 1.16-fold of the 0 mM vehicle control at 0.08, 0.16, and 0.20 mM, respectively (Fig. 5C,D). Together, these results indicate that 20E induces apoptosis-associated changes in glioblastoma cells, although additional cell-death mechanisms cannot be excluded.

### *3.8 20-Hydroxyecdysone Suppresses Colony Formation and Migration*

Because inhibition of short-term proliferation does not necessarily imply a reduction in long-term proliferative potential, we further used colony formation assays to evaluate the effect of 20E on clonal expansion. Representative staining images and quantitative analyses showed that 20E reduced relative colony formation efficiency in both U251 and U87 cells, with more evident inhibition at medium-to-high concentrations. In U251 cells, relative colony formation efficiency was significantly reduced to 65.5%, 60.7%, 55.0%, and 52.4% of the 0 mM vehicle control at 0.08, 0.12, 0.16, and 0.20 mM, respectively. In U87 cells, 20E also significantly reduced colony formation efficiency at 0.08–0.20 mM, with values of 73.4%, 68.4%, 76.6%, and 76.1% of the vehicle control, respectively (Fig. 6A–D).

We next assessed cell migration using a wound-healing assay. In both U251 and U87 cells, 20E produced a concentration-associated reduction in wound closure, and the inhibitory effect became more pronounced at medium-to-high concentrations. In U251 cells, the migration rates in the 0 mM vehicle control group were 34.5%, 46.8%, and 48.0% at 24, 36, and 48 h, respectively. By contrast, treatment with 0.20 mM 20E reduced the migration rates to 0.79%, 1.98%, and 2.38% at the corresponding time points (Fig. 6E–H). In U87 cells, the migration rates in the 0 mM vehicle control group were 30.2%, 55.0%, and 86.9% at 12, 24, and 36 h, respectively, whereas 0.20 mM 20E reduced them to 3.61%, 3.05%, and 24.8%, respectively (Fig. 6I–L). These results indicate that 20E impairs both clonogenic capacity and migratory behavior in glioblastoma cells.

### *3.9 20-Hydroxyecdysone Inhibits Phosphorylation-Dependent Activation of the PI3K/AKT Pathway*

Based on the preceding network pharmacology enrichment analysis and molecular docking results, which suggested that the PI3K/AKT signaling pathway is a key mechanistic axis, we further examined the activation status of this pathway and its downstream node GSK3β at the cellular level. In U251 cells, compared with the 0 mM vehicle control, treatment with 0.12 mM 20E for 24 h significantly reduced the ratios of p-PI3K/PI3K, p-AKT/AKT, and p-GSK3β/GSK3β to 85.2%, 73.4%, and 88.4% of the vehicle control level, respectively. In contrast, total PI3K, AKT, and GSK3β levels normalized to GAPDH were not significantly changed (Fig. 7A–G). These data indicate that 20E mainly affects phosphorylation-dependent activation of the PI3K/AKT/GSK3β axis rather than reducing the total abundance of the related proteins.

A similar pattern was observed in U87 cells. Compared with the 0 mM vehicle control, 0.12 mM 20E significantly reduced the ratios of p-PI3K/PI3K, p-AKT/AKT, and p-GSK3β/GSK3β to 69.9%, 80.2%, and 79.2% of the vehicle control level, respectively, while total PI3K, AKT, and GSK3β expression showed no significant changes (Fig. 7H–N). The consistent pattern observed in both glioma cell lines—suppression of phosphorylation rather than reduction of total protein abundance—supports the conclusion that 20E inhibits phosphorylation-dependent PI3K/AKT/GSK3β pathway activation, in line with its antiproliferative, antimigratory, and apoptosis-associated effects.

## 4. Discussion

The significance of this study lies not only in identifying a natural bioactive molecule of interest, but also in establishing a mechanistic chain that starts from the disease network and returns to the cellular level for experimental validation. Recent reviews generally agree that the difficulty in achieving major therapeutic breakthroughs in GBM is not merely a consequence of rapid tumor growth, but more importantly reflects its high invasiveness, pro-

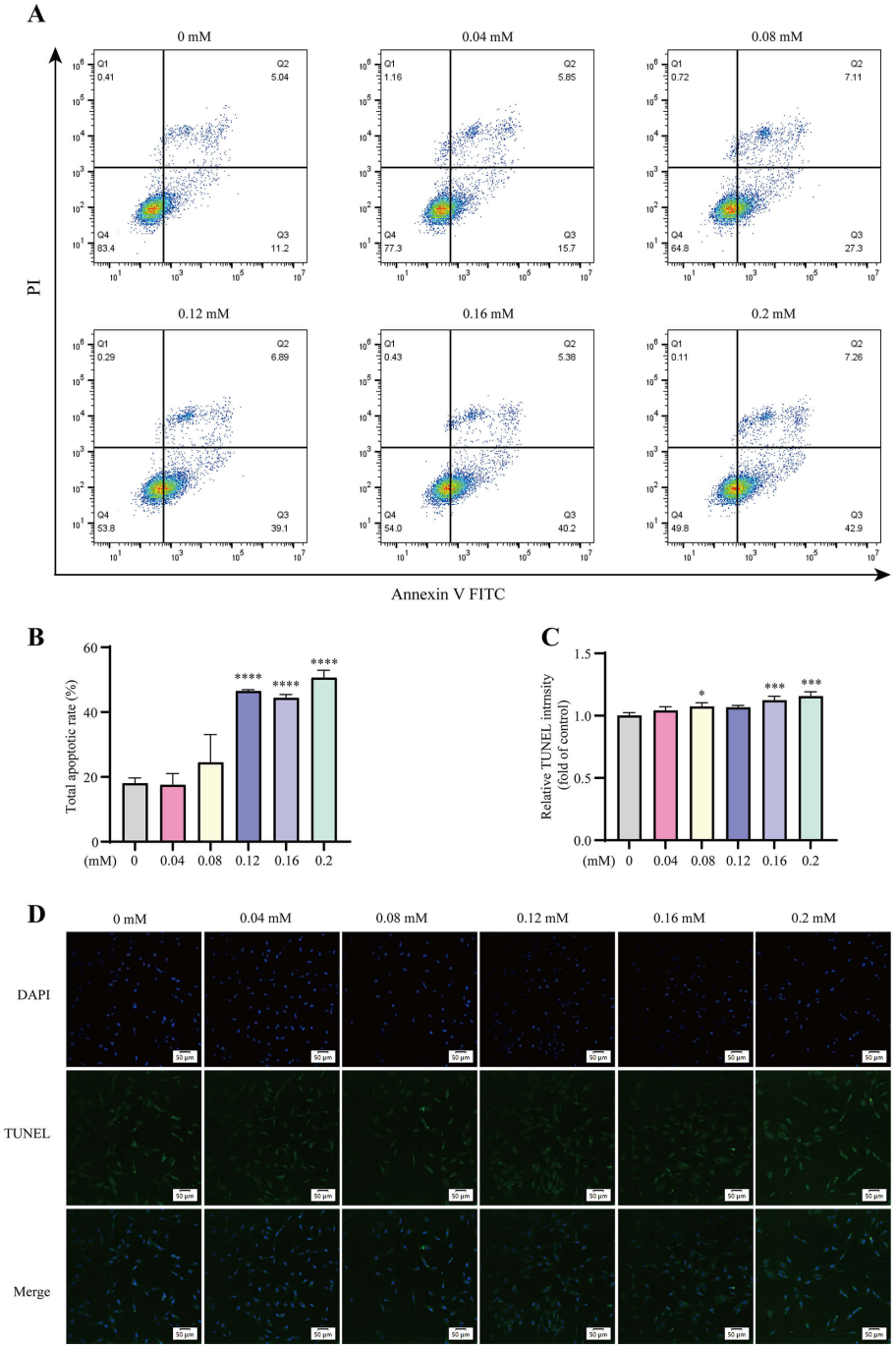


**Fig. 5. 20-Hydroxyecdysone increases apoptosis-associated cell death in glioblastoma cells**. (A) Representative Annexin V-FITC/PI flow cytometry plots of U87 cells after treatment with 0, 0.04, 0.08, 0.12, 0.16, or 0.20 mM 20-hydroxyecdysone (20E) for 24 h. The 0 mM group was treated with the same volume of DMSO and served as the vehicle control. Cross-gates were established based on the unstained blank control and single-stained FITC and PI controls, and the same gating strategy was applied consistently to all treatment groups. Q2 and Q3 represent late and early apoptotic cells, respectively. (B) Quantification of the total apoptotic cell population, defined as Q2 + Q3, based on three independent biological replicates (n = 3). (C) Quantification of relative TUNEL intensity in U251 cells after treatment with the indicated concentrations of 20E. (D) Representative TUNEL staining images of U251 cells after treatment with the indicated concentrations of 20E. Nuclei were stained with DAPI, and TUNEL-positive cells are shown in green. Scale bar = 50 μm. Data are presented as the mean ± SD from three independent biological replicates (n = 3). For comparisons among multiple treatment groups, statistical significance was analyzed using one-way ANOVA followed by Dunnett's multiple comparisons test versus the 0 mM vehicle control group. *$p < 0.05$; ***$p < 0.001$; ****$p < 0.0001$.

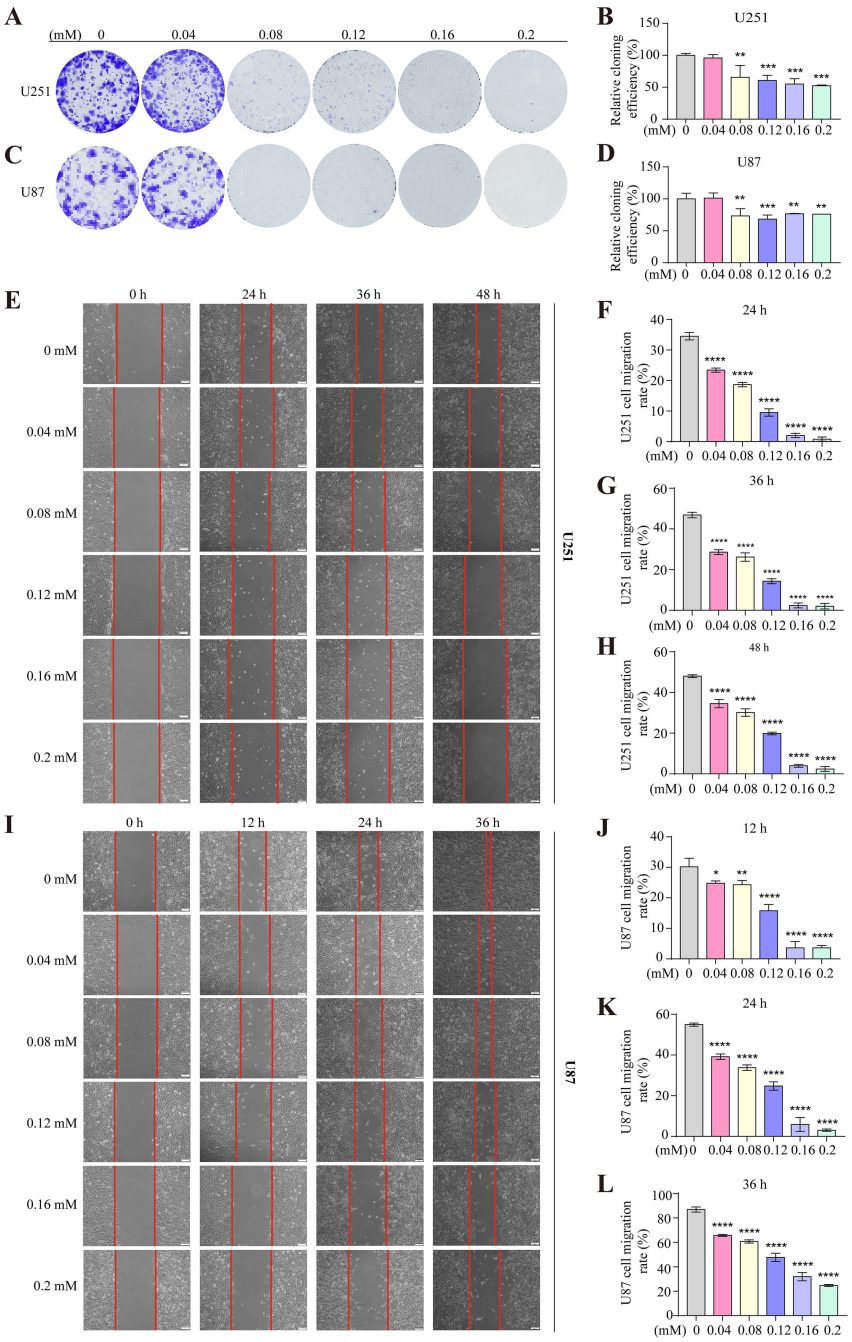


**Fig. 6. 20-Hydroxyecdysone suppresses colony formation and migration of glioblastoma cells**. (A,B) Representative colony formation images and quantification of relative colony formation efficiency in U251 cells after treatment with 0, 0.04, 0.08, 0.12, 0.16, or 0.20 mM 20-hydroxyecdysone. (C,D) Representative colony formation images and quantification of relative colony formation efficiency in U87 cells after treatment with the indicated concentrations of 20-hydroxyecdysone. (E) Representative wound-healing images of U251 cells treated with the indicated concentrations of 20-hydroxyecdysone and photographed at 0, 24, 36, and 48 h after scratching. (F–H) Quantification of U251 cell migration rates at 24, 36, and 48 h, respectively. (I) Representative wound-healing images of U87 cells treated with the indicated concentrations of 20-hydroxyecdysone and photographed at 0, 12, 24, and 36 h after scratching. (J–L) Quantification of U87 cell migration rates at 12, 24, and 36 h, respectively. The 0 mM group was treated with the same volume of DMSO and served as the vehicle control. Scale bar = 100 μm. Data are presented as the mean ± SD from three independent biological replicates (n = 3). For comparisons among multiple treatment groups, statistical significance was analyzed using one-way ANOVA followed by Dunnett's multiple comparisons test versus the 0 mM vehicle control group. *$p < 0.05$; **$p < 0.01$; ***$p < 0.001$; ****$p < 0.0001$.

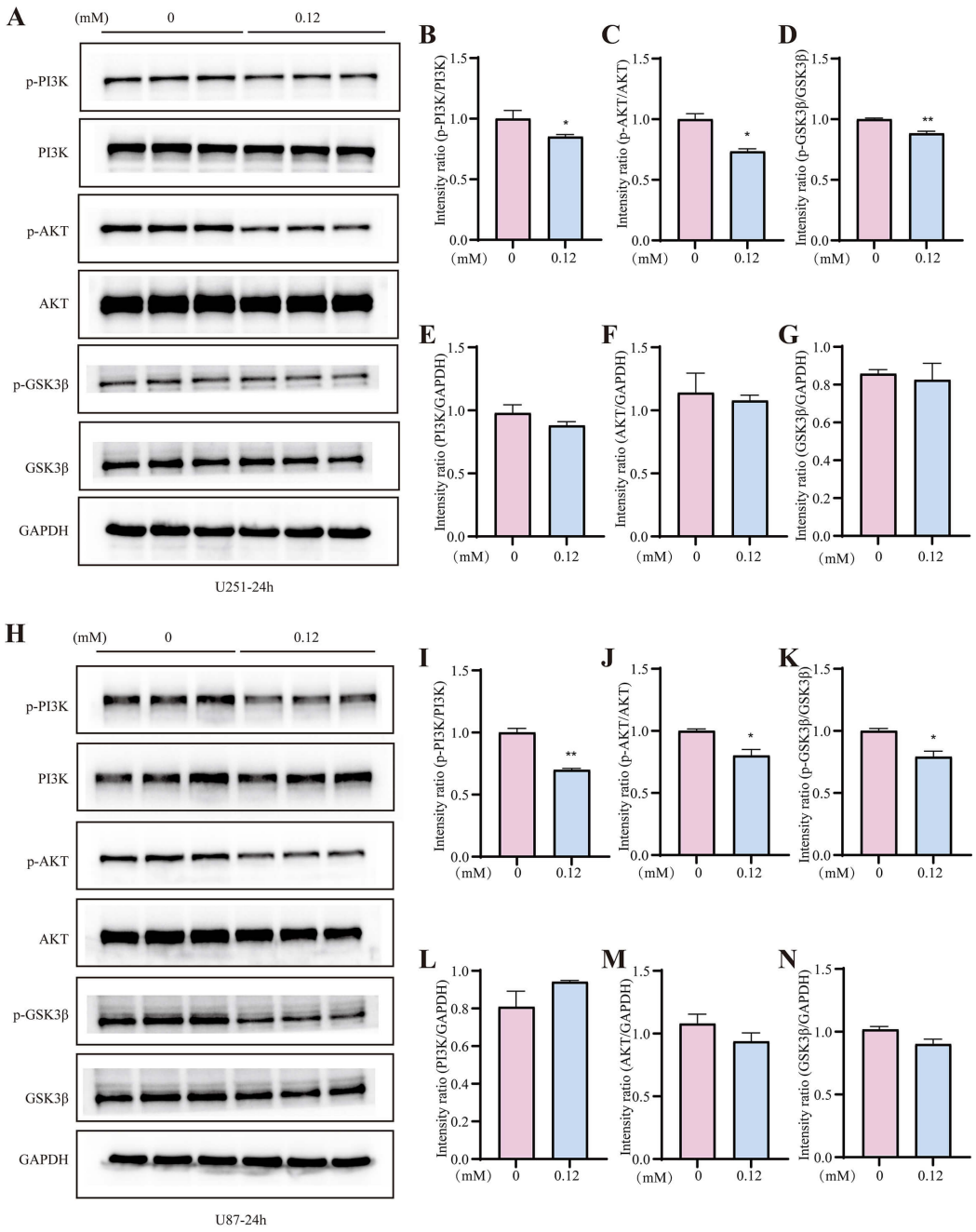


**Fig. 7. 20-Hydroxyecdysone suppresses phosphorylation-dependent activation of the PI3K/AKT/GSK3β signaling pathway in glioblastoma cells**. (A) Representative Western blot images of p-PI3K, PI3K, p-AKT, AKT, p-GSK3β, GSK3β, and GAPDH in U251 cells after treatment with 0 or 0.12 mM 20-hydroxyecdysone for 24 h. (B–D) Quantification of p-PI3K/PI3K, p-AKT/AKT, and p-GSK3β/GSK3β ratios in U251 cells, respectively. (E–G) Quantification of total PI3K/GAPDH, AKT/GAPDH, and GSK3β/GAPDH levels in U251 cells, respectively. (H) Representative Western blot images of p-PI3K, PI3K, p-AKT, AKT, p-GSK3β, GSK3β, and GAPDH in U87 cells after treatment with 0 or 0.12 mM 20-hydroxyecdysone for 24 h. (I–K) Quantification of p-PI3K/PI3K, p-AKT/AKT, and p-GSK3β/GSK3β ratios in U87 cells, respectively. (L–N) Quantification of total PI3K/GAPDH, AKT/GAPDH, and GSK3β/GAPDH levels in U87 cells, respectively. The 0 mM group was treated with the same volume of DMSO and served as the vehicle control. Data are presented as the mean ± SD from three independent biological replicates (n = 3). Statistical significance between two groups was analyzed using paired Student's *t*-test. *$p < 0.05$; **$p < 0.01$.

nounced molecular plasticity, and ability to rapidly rebuild adaptive networks after treatment [22,23,24]. Against this background, rather than starting from predefined pharmacological assumptions, we first extracted disease modules from GBM-related targets and transcriptomic signals, then worked backward to identify 20E, and finally validated its

anti-glioma potential through docking, molecular dynamics, and *in vitro* experiments. Our results showed that 20E inhibited proliferation, colony formation, and migration in U251 and U87 cells while inducing apoptosis-associated changes, supporting its value for further evaluation.

It should also be noted that the viability response was not completely linear at all early or low-dose conditions. In U87 cells, low-dose 20E produced a modest increase in viability at selected time points, whereas this effect was not sustained under higher concentrations or longer treatment durations. This pattern may reflect a transient adaptive or hormetic-like response in this cellular background and should not be interpreted as a sustained pro-proliferative effect. In addition, Annexin V-FITC/PI staining showed PI-positive/Annexin V-low events in some 20E-treated groups, indicating that non-apoptotic or necrotic-like cell death may also contribute under certain conditions.

From a research perspective, we adopted reverse network pharmacology not only to improve screening efficiency, but also to ensure that the selection of candidate molecules remained as close as possible to key disease-associated networks. Network medicine proposes that pathogenic molecules in complex diseases often exist as modules within interaction networks, and that stable phenotypic outputs are usually determined not by a single target but by the connectivity within such modules [25]. Network pharmacology, in turn, provides a practical framework for integrating multicomponent, multitarget, and multipathway information into testable hypotheses [26]. On this basis, combining reverse network pharmacology with virtual reverse pharmacology offers a rational strategy for inferring candidate molecules and targets from disease-related gene sets [27]. This concept also underlies the way we linked bioinformatic screening, PPI hubs, pathway enrichment, and subsequent experimental validation in the present study.

At the mechanistic level, we ultimately focused on the PI3K/AKT signaling axis. This decision was driven not only by the prominence of this pathway in the enrichment results, but also by its ability to account for the multidimensional phenotypic changes we observed. Previous studies have shown that aberrant RTK-associated signaling in GBM often converges on the PI3K/AKT axis, thereby affecting cell survival, metabolic adaptation, and invasive migration [28,29]. Notably, earlier work suggested that migrating glioma cells actively engage PI3K-dependent survival programs, thereby becoming less sensitive to apoptotic stimuli [30]. Accordingly, in our experiments, 20E-induced reductions in cell viability and migration, together with apoptosis-associated changes and decreased p-PI3K/PI3K and p-AKT/AKT ratios, fit well within the logic of this pathway and suggest that 20E acts, at least in part, by weakening this survival–migration coupling axis.

It is also important to note that our molecular docking analysis was not based on arbitrarily selecting a few molecules from a large number of core targets, but was instead centered on 10 candidate targets enriched within the AKT pathway, which makes the docking results biologically more focused. Docking and molecular dynamics analyses indicated that 20E has favorable binding feasibility for nodes such as EGFR, FLT1, and ITGA5, thereby making the hypothesis of multinode action within the AKT pathway more tangible. As reported in the literature, EGFR remains one of the most representative upstream drivers of GBM, and its aberrant activation can continuously fuel downstream PI3K/AKT-related programs [31]. ITGA5 is associated not only with invasive behavior but also with resistance to TMZ and antiangiogenic agents [32,33], whereas the FLT1/ANGPT2 axis suggests that the potential role of 20E may extend beyond intrinsic tumor-cell proliferation signaling to include vascular-related microenvironmental regulation [34]. Moreover, the relationship between ECM-related nodes such as COL6A1 and GBM stemness maintenance or chemotherapy resistance suggests that 20E may ultimately influence a broader tumor niche [35]. At present, however, these structural data are best interpreted as a basis for prioritizing targets and guiding mechanistic inquiry; direct intracellular target engagement still needs to be established.

Among our results, one of the most informative findings linking pathway changes with phenotype is that, in addition to reduced p-PI3K and p-AKT, 20E also decreased the p-GSK3β (Ser9)/GSK3β ratio while leaving total GSK3β unchanged. Because Ser9 is the classical inhibitory phosphorylation site of GSK3β, this result suggests attenuation of inhibitory phosphorylation at GSK3β. Importantly, PI3K/AKT-related signaling has already been linked to TMZ resistance [36,37], and GSK3β itself is recognized as an important node connecting migration, invasion, and stress adaptation [38]. In GBM, GSK3β has been reported to support invasive programs [16] and to be coupled to epithelial–mesenchymal transition (EMT)-like outputs involving β-catenin and Twist [39]. In addition, natural-product studies in U87 and U251 cells have shown that suppression of invasion and migration can occur through the AKT/GSK3β/β-catenin axis [40]. Taken together, these findings suggest that the effect of 20E should not be viewed simply as inhibition of AKT signaling; rather, it may involve reshaping the broader PI3K/AKT–GSK3β continuum, thereby influencing downstream transcriptional and cellular programs related to migration and apoptosis-associated responses. Further investigation of β-catenin stability or nuclear translocation, together with EMT- and invasion-related markers, would help complete this mechanistic chain.

Several issues still warrant further investigation. First, molecular docking and molecular dynamics are used primarily to screen and strengthen mechanistic hypotheses

rather than to directly prove intracellular target occupancy, and their interpretive limits should therefore be acknowledged [41,42]. To further strengthen the argument, cellular thermal shift assay (CETSA) or related target-engagement assays should be incorporated [43,44]. Second, although U87 and U251 are classic and widely used models, their origin and long-term passage drift have repeatedly been discussed in the field [45,46]. Future studies would therefore benefit from the use of systems that more closely reflect clinical heterogeneity, such as patient-derived organoids; indeed, recent work has shown that patient-derived GBM organoids can serve as near-real-time platforms for assessing therapeutic responses [47]. Third, because 20E already has a degree of preclinical safety and pharmacokinetic support [20], and recent reviews have begun to systematically summarize its molecular targets and modes of action in mammals [48], we believe that it has a reasonable basis for further translational development. Nevertheless, drug delivery remains a major challenge in GBM therapy, particularly with respect to increasing effective intratumoral exposure while maintaining acceptable systemic exposure. Accordingly, nanodelivery and related optimization strategies should be considered in future work [49]. Overall, our study provides a solid foundation for further investigation of ecdysone: it emerged from the disease network, converged on a clear AKT-related mechanistic anchor, and consistently displayed anti-GBM activity *in vitro*.

*Limitations*

This study has several limitations. First, the effective concentrations of 20E used *in vitro* were relatively high compared with highly optimized anticancer agents. Therefore, 20E should currently be regarded as a candidate lead compound for proof-of-concept validation, and future work should explore structural optimization, delivery optimization, or combination strategies to improve potency and therapeutic selectivity. Second, molecular docking and molecular dynamics simulations can support target prioritization but cannot prove direct intracellular target engagement. Additional assays such as CETSA, SPR, ITC, or pull-down experiments will be needed to verify direct interactions between 20E and candidate targets. Third, the present experimental validation was mainly based on classical U251 and U87 glioma cell lines. Future studies using patient-derived GBM cells, organoids, and *in vivo* GBM models are required to better evaluate clinical relevance and therapeutic potential.

## 5. Conclusions

In summary, this study identified 20E through reverse network pharmacology screening and, together with molecular docking, molecular dynamics, and *in vitro* experiments, demonstrated that it significantly inhibits glioma cell proliferation, colony formation, and migration while inducing apoptosis-associated changes. Mechanistically, 20E suppresses activation of the PI3K/AKT signaling pathway and is accompanied by decreased downstream GSK3β (Ser9) phosphorylation, suggesting that the PI3K/AKT–GSK3β axis may mediate at least part of its antiglioma effect. These findings provide a basis for further investigation of 20E as a potential candidate intervention for GBM and also offer a useful strategy for discovering natural bioactive compounds and validating their mechanisms through reverse network pharmacology.

## Availability of Data and Materials

The datasets used and analyzed during the current study are available from the corresponding authors on reasonable request.

## Author Contributions

Conceptualization, JZ, CW, DW, JX and JL; methodology, JZ, CW, RH, XX, DW, and JL; software, CW, and JL; validation, JZ, CW, RH, XX and JL; formal analysis, CW; investigation, JZ, CW, JX and JL; resources, JZ, CW, and JL; data curation, JZ, CW, DW, and JL.; writing—original draft preparation, JZ, CW, DW, JX and JL; writing—review and editing, JZ, CW, DW, JX and JL; visualization, JZ, CW, JX and JL; supervision, CW and JL; project administration, JZ, CW, DW, JX and JL; funding acquisition, DW and JL. All authors have read and agreed to the published version of the manuscript. All authors contributed to editorial changes in the manuscript. All authors have participated sufficiently in the work and agreed to be accountable for all aspects of the work.

## Ethics Approval and Consent to Participate

Not applicable.


## Acknowledgment

Not applicable.

## Funding

This work was supported by the Young Scientific Talents Growth Project of the Guizhou Provincial Education Department (Grant No. KY [2022]228), the Doctoral Foundation of Guizhou Medical University (Grant Nos. [2021]020 and 040203), the National Natural Science Foundation Cultivation Project of Guizhou Medical University (Grant Nos. 21NSFCP25 and 22NSFCP09), and the Qiankehe Platform (Project Nos. KXJZ[2024]004 and SSYS[2026]ZD017).


## Conflicts of Interest

The authors declare no conflicts of interest.

## Declaration of AI and AI-Assisted Technologies in the Writing Process

During the preparation of this work, the authors used ChatGPT-3.5 in order to check spelling and grammar. After using this tool, the authors reviewed and edited the content as needed and take full responsibility for the content of the publication.

## References


[1] Price M, Ballard CAP, Benedetti JR, Kruchko C, Barnholtz-Sloan JS, Ostrom QT. CBTRUS Statistical Report: Primary Brain and Other Central Nervous System Tumors Diagnosed in the United States in 2018-2022. Neuro-Oncology. 2025; 27: iv1–iv66. https://doi.org/10.1093/neuonc/noaf194

[2] Louis DN, Perry A, Wesseling P, Brat DJ, Cree IA, Figarella-Branger D, et al. The 2021 WHO Classification of Tumors of the Central Nervous System: a summary. Neuro-Oncology. 2021; 23: 1231–1251. https://doi.org/10.1093/neuonc/noab106

[3] Stupp R, Mason WP, van den Bent MJ, Weller M, Fisher B, Taphoorn MJB, et al. Radiotherapy plus concomitant and adjuvant temozolomide for glioblastoma. The New England Journal of Medicine. 2005; 352: 987–996. https://doi.org/10.1056/NEJMoa043330

[4] Vaz-Salgado MA, Villamayor M, Albarrán V, Alía V, Sotoca P, Chamorro J, et al. Recurrent Glioblastoma: A Review of the Treatment Options. Cancers. 2023; 15: 4279. https://doi.org/10.3390/cancers15174279

[5] Sharma P, Aaroe A, Liang J, Puduvalli VK. Tumor microenvironment in glioblastoma: Current and emerging concepts. Neuro-Oncology Advances. 2023; 5: vdad009. https://doi.org/10.1093/noajnl/vdad009

[6] Newman DJ, Cragg GM. Natural Products as Sources of New Drugs over the Nearly Four Decades from 01/1981 to 09/2019. Journal of Natural Products. 2020; 83: 770–803. https://doi.org/10.1021/acs.jnatprod.9b01285

[7] Hopkins AL. Network pharmacology. Nature Biotechnology. 2007; 25: 1110–1111. https://doi.org/10.1038/nbt1007-1110

[8] Hopkins AL. Network pharmacology: the next paradigm in drug discovery. Nature Chemical Biology. 2008; 4: 682–690. https://doi.org/10.1038/nchembio.118

[9] Chandran U, Mehendale N, Patil S, Chaguturu R, Patwardhan B. Network Pharmacology. In Patwardhan B, Chaguturu R (eds.) Innovative Approaches in Drug Discovery (pp. 127–164). Academic Press: Boston. 2017. https://doi.org/10.1016/B978-0-12-801814-9.00005-2

[10] Kong X, Liu C, Zhang Z, Cheng M, Mei Z, Li X, et al. BATMAN-TCM 2.0: an enhanced integrative database for known and predicted interactions between traditional Chinese medicine ingredients and target proteins. Nucleic Acids Research. 2024; 52: D1110–D1120. https://doi.org/10.1093/nar/gkad926

[11] Dinan L, Dioh W, Veillet S, Lafont R. 20-Hydroxyecdysone, from Plant Extracts to Clinical Use: Therapeutic Potential for the Treatment of Neuromuscular, Cardio-Metabolic and Respiratory Diseases. Biomedicines. 2021; 9: 492. https://doi.org/10.3390/biomedicines9050492

[12] Shuvalov O, Kirdeeva Y, Fefilova E, Netsvetay S, Zorin M, Vlasova Y, et al. 20-Hydroxyecdysone Confers Antioxidant and Antineoplastic Properties in Human Non-Small Cell Lung Cancer Cells. Metabolites. 2023; 13: 656. https://doi.org/10.3390/metabo13050656

[13] Ma Q, Wu F, Liu X, Zhao C, Sun Y, Li Y, et al. 20-hydroxyecdysone suppresses bladder cancer progression via inhibiting USP21: A mechanism associated with deubiquitination and degradation of p65. Translational Oncology. 2024; 45: 101958. https://doi.org/10.1016/j.tranon.2024.101958

[14] Martins A, Sipos P, Dér K, Csábi J, Miklos W, Berger W, et al. Ecdysteroids sensitize MDR and non-MDR cancer cell lines to doxorubicin, paclitaxel, and vincristine but tend to protect them from cisplatin. BioMed Research International. 2015; 2015: 895360. https://doi.org/10.1155/2015/895360

[15] Majewska E, Szeliga M. AKT/GSK3β Signaling in Glioblastoma. Neurochemical Research. 2017; 42: 918–924. https://doi.org/10.1007/s11064-016-2044-4

[16] Chikano Y, Domoto T, Furuta T, Sabit H, Kitano-Tamura A, Pyko IV, et al. Glycogen synthase kinase 3β sustains invasion of glioblastoma via the focal adhesion kinase, Rac1, and c-Jun N-terminal kinase-mediated pathway. Molecular Cancer Therapeutics. 2015; 14: 564–574. https://doi.org/10.1158/1535-7163.MCT-14-0479

[17] Minegishi K, Dobashi Y, Kimura E, Goto A. AKT: A Central Node in Complex Signaling Cascades. Frontiers in Bioscience (Landmark Edition). 2025; 30: 26414. https://doi.org/10.31083/fbl26414

[18] Zhao B, Shen C, Zheng Z, Wang X, Zhao W, Chen X, et al. Peiminine Inhibits Glioblastoma in Vitro and in Vivo Through Cell Cycle Arrest and Autophagic Flux Blocking. Cellular Physiology and Biochemistry: International Journal of Experimental Cellular Physiology, Biochemistry, and Pharmacology. 2018; 51: 1566–1583. https://doi.org/10.1159/000495646

[19] Carrillo-Beltrán D, Nahuelpan Y, Cuevas C, Fabres K, Silva P, Zubieta J, et al. Glycosylated Delphinidins Decrease Chemoresistance to Temozolomide by Regulating NF-κB/MGMT Signaling in Glioblastoma. Cells. 2025; 14: 179. https://doi.org/10.3390/cells14030179

[20] Dioh W, Tourette C, Del Signore S, Daudigny L, Dupont P, Balducci C, et al. A Phase 1 study for safety and pharmacokinetics of BIO101 (20-hydroxyecdysone) in healthy young and older adults. Journal of Cachexia, Sarcopenia and Muscle. 2023; 14: 1259–1273. https://doi.org/10.1002/jcsm.13195

[21] Romaniuk-Drapała A, Lisiak N, Totoń E, Matysiak A, Nawrot J, Nowak G, et al. Proapoptotic and proautophagic activity of 20-hydroxyecdysone in breast cancer cells in vitro. Chemico-Biological Interactions. 2021; 342: 109479. https://doi.org/10.1016/j.cbi.2021.109479

[22] Singh S, Dey D, Barik D, Mohapatra I, Kim S, Sharma M, et al. Glioblastoma at the crossroads: current understanding and future therapeutic horizons. Signal Transduction and Targeted Therapy. 2025; 10: 213. https://doi.org/10.1038/s41392-025-02299-4

[23] Shetty C, Tamatta R, Dhas N, Singh AK. Evolving therapeutic strategies in glioblastoma: traditional approaches and novel interventions. 3 Biotech. 2025; 15: 318. https://doi.org/10.1007/s13205-025-04493-1

[24] Kurdi M, Bamaga A, Alkhotani A, Alsharif T, Abdel-Hamid GA, Selim ME, et al. Mitochondrial DNA Alterations in Glioblastoma and Current Therapeutic Targets. Frontiers in Bioscience (Landmark Edition). 2024; 29: 367. https://doi.org/10.31083/j.fbl2910367

[25] Barabási AL, Gulbahce N, Loscalzo J. Network medicine: a network-based approach to human disease. Nature Reviews. Genetics. 2011; 12: 56–68. https://doi.org/10.1038/nrg2918

[26] Nogales C, Mamdouh ZM, List M, Kiel C, Casas AI, Schmidt HHHW. Network pharmacology: curing causal mechanisms instead of treating symptoms. Trends in Pharmacological Sciences. 2022; 43: 136–150. https://doi.org/10.1016/j.tips.2021.11.004

[27] Lagunin AA, Ivanov SM, Gloriozova TA, Pogodin PV, Filimonov DA, Kumar S, et al. Combined network pharmacology and virtual reverse pharmacology approaches for identification

of potential targets to treat vascular dementia. Scientific Reports. 2020; 10: 257. https://doi.org/10.1038/s41598-019-57199-9

[28] Qin A, Musket A, Musich PR, Schweitzer JB, Xie Q. Receptor tyrosine kinases as druggable targets in glioblastoma: Do signaling pathways matter? Neuro-Oncology Advances. 2021; 3: vdab133. https://doi.org/10.1093/noajnl/vdab133

[29] Manning BD, Toker A. AKT/PKB Signaling: Navigating the Network. Cell. 2017; 169: 381–405. https://doi.org/10.1016/j.cell.2017.04.001

[30] Joy AM, Beaudry CE, Tran NL, Ponce FA, Holz DR, Demuth T, et al. Migrating glioma cells activate the PI3-K pathway and display decreased susceptibility to apoptosis. Journal of Cell Science. 2003; 116: 4409–4417. https://doi.org/10.1242/jcs.00712

[31] Ezzati S, Salib S, Balasubramaniam M, Aboud O. Epidermal Growth Factor Receptor Inhibitors in Glioblastoma: Current Status and Future Possibilities. International Journal of Molecular Sciences. 2024; 25: 2316. https://doi.org/10.3390/ijms25042316

[32] Shi Y, Wu M, Liu Y, Hu L, Wu H, Xie L, et al. *ITGA5* Predicts Dual-Drug Resistance to Temozolomide and Bevacizumab in Glioma. Frontiers in Oncology. 2021; 11: 769592. https://doi.org/10.3389/fonc.2021.769592

[33] Feng L, Ma J, Ji H, Liu Y, Hu W. miR-330-5p suppresses glioblastoma cell proliferation and invasiveness by targeting ITGA5. Oncology Reports. 2017; 38: 1749–1757. https://doi.org/10.3892/or.2017.5827

[34] Peterson TE, Kirkpatrick ND, Huang Y, Farrar CT, Marijt KA, Kloepper J, et al. Dual inhibition of Ang-2 and VEGF receptors normalizes tumor vasculature and prolongs survival in glioblastoma by altering macrophages. Proceedings of the National Academy of Sciences of the United States of America. 2016; 113: 4470–4475. https://doi.org/10.1073/pnas.1525349113

[35] Cescon M, Rampazzo E, Bresolin S, Da Ros F, Manfreda L, Cani A, et al. Collagen VI sustains cell stemness and chemotherapy resistance in glioblastoma. Cellular and Molecular Life Sciences: CMLS. 2023; 80: 233. https://doi.org/10.1007/s00018-023-04887-5

[36] Zając A, Sumorek-Wiadro J, Langner E, Wertel I, Maciejczyk A, Pawlikowska-Pawlęga B, et al. Involvement of PI3K Pathway in Glioma Cell Resistance to Temozolomide Treatment. International Journal of Molecular Sciences. 2021; 22: 5155. https://doi.org/10.3390/ijms22105155

[37] Zhang H, Liu Z, Cheng J, Jiang Y, Zheng X, Zhang C, et al. HTR1D regulates the PI3K/Akt signaling pathway to impact glioblastoma development and resistance to temozolomide. Chemico-biological Interactions. 2025; 421: 111748. https://doi.org/10.1016/j.cbi.2025.111748

[38] Domoto T, Uehara M, Bolidong D, Minamoto T. Glycogen Synthase Kinase 3β in Cancer Biology and Treatment. Cells. 2020; 9: 1388. https://doi.org/10.3390/cells9061388

[39] Yang W, Wu PF, Ma JX, Liao MJ, Wang XH, Xu LS, et al. Sortilin promotes glioblastoma invasion and mesenchymal transition through GSK-3β/β-catenin/twist pathway. Cell Death & Disease. 2019; 10: 208. https://doi.org/10.1038/s41419-019-1449-9

[40] Zhang X, Zheng K, Li C, Zhao Y, Li H, Liu X, et al. Nobiletin inhibits invasion via inhibiting AKT/GSK3β/β-catenin signaling pathway in Slug-expressing glioma cells. Oncology Reports. 2017; 37: 2847–2856. https://doi.org/10.3892/or.2017.5522

[41] Chen YC. Beware of docking! Trends in Pharmacological Sciences. 2015; 36: 78–95. https://doi.org/10.1016/j.tips.2014.12.001

[42] Hollingsworth SA, Dror RO. Molecular Dynamics Simulation for All. Neuron. 2018; 99: 1129–1143. https://doi.org/10.1016/j.neuron.2018.08.011

[43] Martinez Molina D, Jafari R, Ignatushchenko M, Seki T, Larsson EA, Dan C, et al. Monitoring drug target engagement in cells and tissues using the cellular thermal shift assay. Science (New York, N.Y.). 2013; 341: 84–87. https://doi.org/10.1126/science.1233606

[44] Jafari R, Almqvist H, Axelsson H, Ignatushchenko M, Lundbäck T, Nordlund P, et al. The cellular thermal shift assay for evaluating drug target interactions in cells. Nature Protocols. 2014; 9: 2100–2122. https://doi.org/10.1038/nprot.2014.138

[45] Allen M, Bjerke M, Edlund H, Nelander S, Westermark B. Origin of the U87MG glioma cell line: Good news and bad news. Science Translational Medicine. 2016; 8: 354re3. https://doi.org/10.1126/scitranslmed.aaf6853

[46] Torsvik A, Stieber D, Enger PØ, Golebiewska A, Molven A, Svendsen A, et al. U-251 revisited: genetic drift and phenotypic consequences of long-term cultures of glioblastoma cells. Cancer Medicine. 2014; 3: 812–824. https://doi.org/10.1002/cam4.219

[47] Logun M, Wang X, Sun Y, Bagley SJ, Li N, Desai A, et al. Patient-derived glioblastoma organoids as real-time avatars for assessing responses to clinical CAR-T cell therapy. Cell Stem Cell. 2025; 32: 181–190.e4. https://doi.org/10.1016/j.stem.2024.11.010

[48] Zádor E. Molecular Targets of 20-Hydroxyecdysone in Mammals, Mechanism of Action: Is It a Calorie Restriction Mimetic and Anti-Aging Compound? Cells. 2025; 14: 431. https://doi.org/10.3390/cells14060431

[49] Rahman MA, Jalouli M, Yadab MK, Al-Zharani M. Progress in Drug Delivery Systems Based on Nanoparticles for Improved Glioblastoma Therapy: Addressing Challenges and Investigating Opportunities. Cancers. 2025; 17: 701. https://doi.org/10.3390/cancers17040701